Journal of Hazardous Materials 215–216 (2012) 25–31

Contents lists available at SciVerse ScienceDirect

Journal of Hazardous Materials

journal homepage: www.elsevier.com/locate/jhazmat

CFD modeling of a UV-LED photocatalytic odor abatement process in a continuous reactor

Zimeng Wang[1], Jing Liu, Yuancan Dai, Weiyang Dong, Shicheng Zhang*, Jianmin Chen**

Department of Environmental Science and Engineering, Fudan University, Shanghai 200433, China

ARTICLE INFO

Article history:
Received 26 September 2011
Received in revised form 2 January 2012
Accepted 8 February 2012
Available online 16 February 2012

Keywords:
Photocatalysis
Computational fluid dynamics
Radiation field model
Kinetics
Light-emitting-diodes
Deodorization

ABSTRACT

This paper presents a model study of a UV light-emitting-diode (UV-LED) based photocatalytic odor abatement process. It integrated computational fluid dynamics (CFD) modeling of the gas flow in the reactor with LED-array radiation field calculation and Langmuir–Hinshelwood reaction kinetics. It was applied to simulate the photocatalytic degradation of dimethyl sulfide (DMS) in a UV-LED reactor based on experimentally determined chemical kinetic parameters. A non-linear power law relating reaction rate to irradiation intensity was adopted. The model could predict the steady state DMS concentration profiles by calculating the advection, diffusion and Langmuir–Hinshelwood reaction kinetics. By affecting the radiation intensity and uniformity, the position of the LED array relative to the catalyst appeared to be a critical parameter determining DMS removal efficiency. Too small distances might yield low quantum efficiency and consequently poor abatement performance. This study provided an example of LED-based photocatalytic process modeling and gave insights into the optimization of light source design for photocatalytic applications.

1. Introduction

Odor pollution from wastewater treatment, landfill, livestock and paper production plants has posed serious environmental and health concerns. Many of the odorous pollutants have extremely low odor thresholds (<100 ppb) and are irritant to eyes, skin and respiratory systems. Repeated exposure to odorous pollution can lead to chronic respiratory and cardiovascular diseases. A number of advanced technologies for the abatement of odorous pollution have been developed, such as active carbon adsorption, activated sludge, biofiltration and incineration [1]. However, these technologies are to some extent limited by either removal efficiency or operating cost [2].

Semiconductor-mediated photocatalytic oxidation (PCO) is a promising technology for odor abatement [3,4], which can be carried out at ambient temperatures without extra addition of oxidant chemicals [5]. Nevertheless, one of the challenges in the commercialization of PCO technology in air purification industry is the limitation of reliable tools to assist the design, optimization, and scale-up of photocatalytic reactors [6]. Empirical or trail-and-error methods are not able to efficiently provide an understanding of the capability and the limitations of the reactors. Recent reports demonstrated that computational fluid dynamics (CFD) is a powerful tool to model the advection, molecular diffusion and chemical reactions in flow through photocatalytic reactors [7–15]. Compared with ordinary chemical reactors, photocatalytic reactors involve particular considerations of the irradiation designs. Therefore, it is crucial to develop models that can help the optimization of the radiation field [16,17]. A number of experimental studies have established the effect of the radiation intensity on the intrinsic reaction kinetics of photocatalytic process [18–20]. However, comprehensive models, which integrate the transport, heterogeneous reaction kinetics and radiation field that can predict the odor abatement as a function of operating parameters in real reactors, are much less common [6].

Most existing photocatalytic studies and applications are using germicidal lamps and fluorescent black-light lamps [3]. However, these traditional UV sources are limited by shortcomings related to sustainability and the environment [21]. Light-emitting-diodes (LEDs) recently became a promising alternative UV source for photocatalytic applications for their high energy efficiency, long lifetime, compact size and DC power supply availability [22,23]. Several recent studies have illustrated that LEDs offer a practical and competitive alternative light source for PCO

* Corresponding author. Tel.: +86 21 65642297; fax: +86 21 65642297.
** Corresponding author. Tel.: +86 21 65642298; fax: +86 21 65642080.
E-mail addresses: zhangsc@fudan.edu.cn (S. Zhang), jmchen@fudan.edu.cn (J. Chen).
[1] Department of Energy, Environmental and Chemical Engineering, Washington University, St. Louis, MO 63130, United States.

0304-3894/$ – see front matter © 2012 Elsevier B.V. All rights reserved.
doi:10.1016/j.jhazmat.2012.02.021

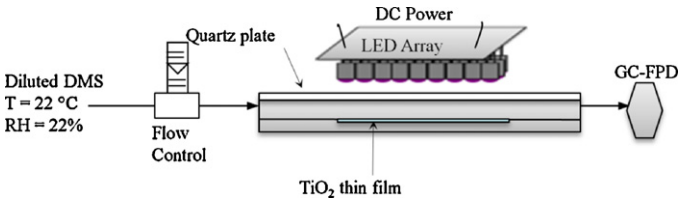

Fig. 1. Schematic sketch of the UV-LED based photocatalytic reactor for DMS abatement.

processes [21–30]. However, to the best of our knowledge, no study on LED-based photocatalytic reactor modeling has been reported.

In this paper, a simple and robust model is developed based on CFD, which couples radiation field model of UV-LED array and photocatalytic reaction kinetics. Dimethyl sulfide (DMS), a representative odorous compound from various anaerobic decay processes [31,32], was chosen as a model pollutant. The flow and concentration profile of DMS in the reactor and the effect of LED array position were calculated in the simulation. These modeling results provide useful information for the design, optimization and scale-up of UV-LED based photocatalytic deodorization processes.

2. Experimental

As shown in Fig. 1, the experimental setup consisted of a narrow slit, plat-plate flow-through reactor. A 25 mm × 60 mm glass plate coated with TiO_2 photocatalyst (P25, Degussa) was embedded into the bottom surface of the reactor. A gas flow channel was made between the catalyst film, and a quartz plate which served as the top cover of the reactor. The flow passage was 5 mm in height and the effective volume of the reactor was 7.5 mL. The reactor inlet and outlet were designed to minimize back-flow and to enable the flow to be fully developed prior to reaching the photocatalyst thin film. DMS at desired concentration was prepared by continuously mixing concentrated standard DMS (50 ppm) gas with synthetic air. A water-bubbling humidifier and a thermohygrometer were used to adjust and monitor the relative humidity of the gas mixture. The experiments were conducted at room temperature (22 ± 2 °C). The relative humidity of the gas mixtures in the reactor was controlled at 22 ± 2%, at which the highest conversion of DMS was reported in a previous study [33]. The concentration of DMS was measured by a gas chromatography (GC) with a flame photometric detector (FPD).

The UV-LEDs used in this work were p–n junction devices made of indium gallium nitride (Yuan-Chuang Electronic, China). It has a peak wavelength at 365 nm with a 10-nm half height width. The directivity of these LEDs is 20° for 50% irradiation energy. The individual lamps were assembled into a 3 × 9 LED array. The LED array, whose dimensions were designed to match that of the TiO_2 coated glass plate, was placed directly above photocatalyst thin film. Irradiance was measured with a spectroradiometer (International Light, Peabody, MA). The detailed information about the catalyst film preparation, experimental protocol and UV-LED characterization was presented in a previous publication [34].

3. Photocatalytic reactor modeling

3.1. Radiation field model

The radiation model in this study was developed considering the unique radiation characteristic of LED lamp using a similar method described by Salvadó-Estivill et al. [7]. Other optical effects, such as scattering and reflection were assumed to be negligible for the narrow-slit gaseous reactor [35]. Due to the directivity of the LED lamps, the photon flux overlapping can significantly affect the radiation field when individual lamps are compactly assembled to be arrays. Fig. 2a shows the relative irradiance as a function of radiation angle in polar coordinates, denoted by $f(\theta)$ ($0 \le \theta < \pi/2$, $0 < f(\theta) \le 1$) in the radiation field model. Based on the geometric relationship shown in Fig. 2b, the relative incident irradiance at certain position on the catalyst can be developed as follows:

$$d = \overline{SO} = \overline{SB} \tag{1}$$

$$\theta = \arctan \frac{\sqrt{(x_0 - x_A)^2 + (y_0 - y_A)^2}}{d} \tag{2}$$

$$I_B = I_o f(\theta) \tag{3}$$

$$\frac{I'_A}{I_B} = \left(\frac{\overline{SB}}{\overline{SA}}\right)^2 = \cos^2(\theta) = \left(\frac{d}{\sqrt{d^2 + (x_0 - x_A)^2 + (y_0 - y_A)^2}}\right)^2 \tag{4}$$

$$I_A = I'_A \cos(\theta) = I_B \cos^3(\theta) = I_o f(\theta) \cos^3(\theta) \tag{5}$$

Eq. (5) can calculate the relative irradiance distribution on a predefined surface as a function of position (x, y) and distance (d) between the surface and a single LED lamp at (x_0, y_0). In order to quantify the irradiance distribution, the irradiance of a single UV-LED was experimentally measured at d = 1.0 cm. The experimental observation and calculated relative irradiance distribution both showed that the photon flux was completely incident to the

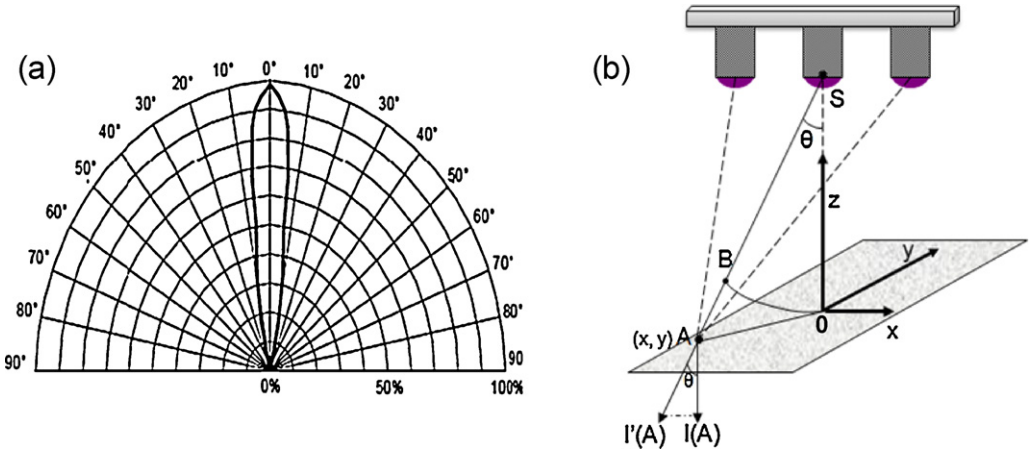

Fig. 2. (a) Radiation directivity of the 365 nm LED lamp, in polar coordinates. (Courtesy of Yuan-Chuang Electronics) (b) Schematic sketch of the irradiation intensity calculation.

detector sensor of the radiometer (radius 0.45 cm). Assuming that the experimentally measured intensity (1.17 mW cm^{-2}) is the average value on the sensor, the total photon power incident was $1.17 \times \pi \times 0.45^2 = 0.75$ mW. The maximum irradiance $I_{O,d=1}$ can be obtained as follows

$$\iint\limits_{\sqrt{x^2+y^2}\le 0.45} I_o^{d=1} f\left(\arctan\frac{\sqrt{x^2+y^2}}{d}\right) \times \left(\frac{d}{\sqrt{d^2+x^2+y^2}}\right)^3 dxdy = 0.75 \quad (6)$$

from which $I_{O,d=1}$ was calculated to be 6.14 mW cm^{-2}.

Consequently, according to the model derivation above, the irradiance at any position (x, y) and distance (d) contributed by a single LED lamp at (x, y) is

$$I(x,y) = \frac{I_o^{d=1}}{d^2} f\left(\arctan\frac{\sqrt{(x_0-x)^2+(y_0-y)^2}}{d}\right) \times \left(\frac{d}{\sqrt{d^2+(x_0-x)^2+(y_0-y)^2}}\right)^3 \quad (7)$$

For multiple LED lamps, it is assumed that each lamp at (x_i, y_i) has identical irradiation property, so that the incident irradiance on the surface of the photocatalyst is equal to the sum of the contribution from each lamp. It follows

$$I(x,y) = \sum_{i=0}^{i=N=27} \frac{I_o^{d=1}}{d^2} f\left(\arctan\frac{\sqrt{(x_i-x)^2+(y_i-y)^2}}{d}\right) \times \left(\frac{d}{\sqrt{d^2+(x_i-x)^2+(y_i-y)^2}}\right)^3 \quad (8)$$

3.2. Transport and kinetics model

The numerical model of the fluid flowing through the reactor involves the solution of the Navier–Stokes equations. The CFD simulations were conducted using Fluent 6.2 (Fluent Inc.). Gambit 2.2 was used to develop a simplified geometric model of the reactor, in which the influent and effluent tubing was not considered in computation. The 3-D domain was discretized into 1 million hexahedral volume cells using standard grid generation method, and they were verified to give mesh-independent results.

The conservation of mass is described by the equation of continuity,

$$\frac{\partial \rho}{\partial t} + \nabla \cdot \rho \mathbf{v} = 0 \quad (9)$$

where t is time, ρ is the density and $\mathbf{v}$ is the velocity vector of the fluid. The conservation of momentum is described by the equation of motion for a horizontal system,

$$\frac{\partial \rho \mathbf{v}}{\partial t} + \nabla \cdot \rho \mathbf{v}\mathbf{v} = -\nabla p - \nabla \cdot \boldsymbol{\tau} \quad (10)$$

where p is the pressure and $\boldsymbol{\tau}$ is the stress tensor defined by Newton's law of viscosity.

The general equation of continuity for species α in terms of $\mathbf{j}_\alpha$ is:

$$\frac{\partial \rho x_\alpha}{\partial t} + \nabla \cdot \rho \mathbf{v} x_\alpha = -\nabla \cdot \mathbf{j}_\alpha + r_\alpha (\mathrm{MW})_\alpha \quad (11)$$

where x_α is the molar fraction of the species α, $(\mathrm{MW})_\alpha$ is its molecular weight, $\mathbf{j}_\alpha$ is the diffusion flux based on the Fick's law and r_α is the net rate of generation of the species α. TiO_2 mediated photocatalytic reactions occurs on the surface of the catalyst. The reaction rate term in Eq. (11) was included to calculate the surface reaction. Under normal circumstances, it should not appear and the reaction term should be introduced as a boundary condition [7,16].

Langmuir–Hinshelwood(L–H) kinetics is widely applicable to model the photocatalytic oxidation of organic gaseous compounds [36]. Our previous study found that DMS photocatalytc oxidation kinetics also followed L–H model [34]. In this work, we extended the rate equation to include the effect of irradiation intensity (I),

$$r = I^\alpha \frac{kKCs}{1+KCs} \quad (12)$$

where C_S is the DMS concentration in the control volumes bordering the surface of the catalyst, K (m^3 mol^{-1}) is the Langmuir adsorption constant and k (mol m^{-3} s^{-1}) is the apparent rate constant. Both constants in this model were obtained based on previous experiments conducted in reaction controlled regime [34]. The apparent rate constant was experimentally determined given per unit catalyst surface area (mol m^{-2} s^{-1}). The radiation field was computed externally based on Eq. (8) and then introduced in the computation by using user-defined functions (UDF). In the 3-dimentional CFD model, the reaction was considered to occur in the layer of control volumes adjacent the surface of the catalyst only, at a rate that was equivalent to that of the surface reaction. In the rest of the cells the last term in Eq. (11) was always zero [7].

Photocatalytic reaction occurs in several regimes in association with irradiation intensity due to the change of the efficiency of electron-hole generation and recombination. The reaction rate increases linearly with absorbed irradiation intensity until a certain value and then increases as the square root of the irradiation intensity [37]. This phenomenon can be explained by a predominant recombination of electron-hole pairs versus charge transfer in oxidation reactions [8,38,39]. A power law was observed in a number of experimental studies [18,20] and has been implemented into a modified L–H kinetic model as shown in Eq. (12) [7,40]. The exponent α varies from one to zero as incident irradiation intensity(I) increases. One-sun equivalent illumination level is often observed as the transition point between the first-order and one-half-order regimes [18]. Consistently, for 365 nm LEDs, our previous experiments founded that the transition of the α values occurred around 1.0 mW cm^{-2} [34]. In the model, a simple mathematical form of power law was adopted:

$$\alpha = \begin{cases} 1.0 & (0 < I \le 1\,\mathrm{mW\ \ cm^{-2}}) \\ 0.5 & (1\,\mathrm{mW\ \ cm^{-2}} < I) \end{cases} \quad (13)$$

At sufficiently weak intensities, the modeled reaction rate is linearly proportional to the irradiation intensity, and shifts to half-order above 1.0 mW cm^{-2}.

Considering the substantially low range of the Reynolds numbers (below 2.75), the simulation in this study was based on laminar flow. Velocity-inlet and outflow were specified as the inlet and outlet boundary conditions, respectively. Second-order upwind discretization scheme was employed. The governing equations were numerically solved by a segregated implicit steady state solution algorithm. The convergence criterion of 10^{-4} was selected for the DMS concentration and other continuity and momentum variables. The diffusion coefficient of TCE in air was estimated to be 1.05×10^{-5} m^2 s^{-1} according to a semi-empirical method of Fuller et al. [41].

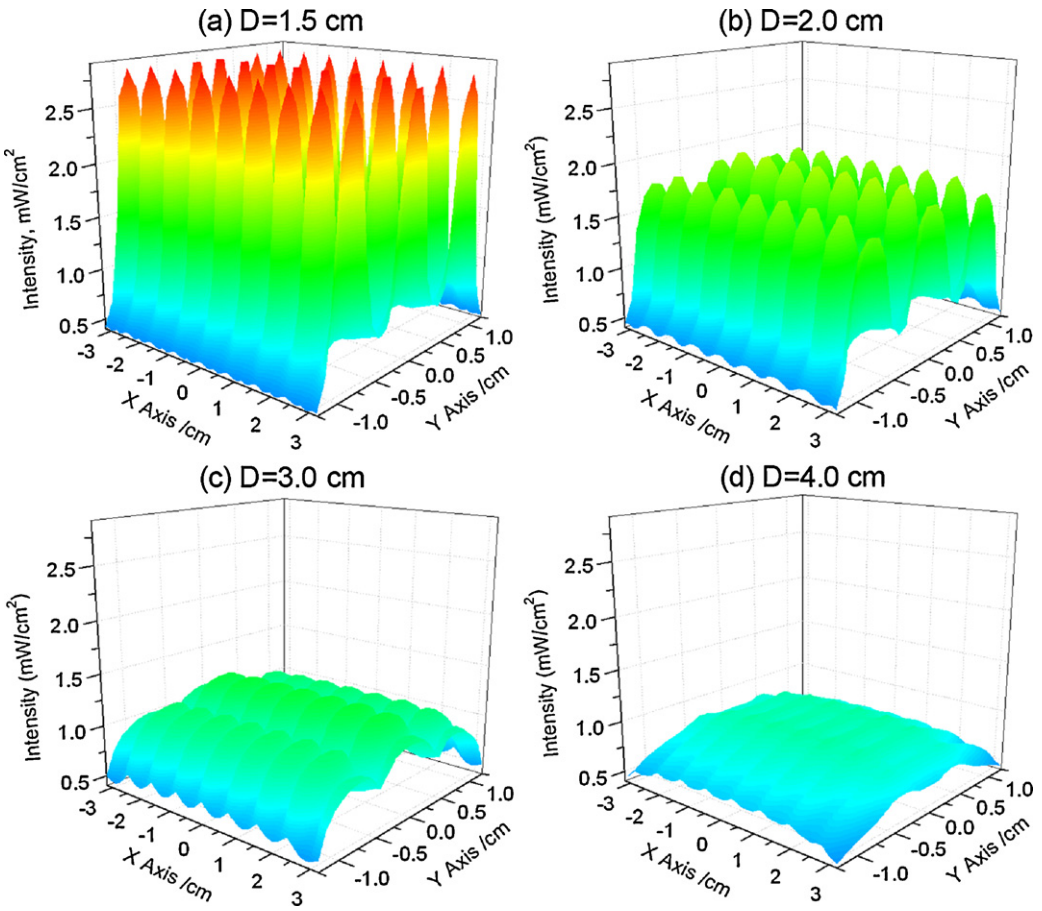

Fig. 3. Model prediction of the radiation intensity distribution on the surface of the catalyst for different LED positions relative to the catalyst surface.

4. Results and discussion

4.1. Modeling the radiation field on the photocatalyst

Fig. 3 shows the model calculations of the radiation distribution on the catalyst plate for different distances between the catalyst surface and the LED array. Due to the small radiation angle of the LED used in this study, the position of the LED array relative to the catalyst surface strongly affects both radiation intensity and uniformity. The closer the lamp to the surface, the less uniform illumination field was formed with 27 strong and distinct light spots on the catalyst surface. Increasing the distance between the LED array and the catalyst, yielded a more homogenous irradiation, however, the radiation intensity inevitably decreased due to the dispersion of photon flux.

Fig. 4 plots the model prediction and experimental measurements of the average and standard deviation of the irradiance on the catalyst surface for different distances between the LED array and the catalyst plate. The experimentally detected average irradiances and standard deviations showed good agreements with the model prediction. The standard deviation of the irradiance decreased dramatically with larger distance due to the effective overlapping of irradiation emitted from individual LED lamps. The average irradiance decreased with larger distance. However, below $D = 3.0$ cm, the average irradiance on the catalyst surface was not inversely proportional to the square of distance. At sufficiently small distances, all of the emitted radiation energy could be confined on the catalyst-coated area, because of the narrow radiation angle of the individual LEDs. Therefore, an optimal range of distances should exist at which a good homogeneity of radiation field can be achieved without losing too much total incident radiation energy. For example, compared with the case for $D = 1.5$ cm, the standard deviation for $D = 3.0$ cm decreased by 70%, while the average irradiance only reduced by 12%. In addition, the irradiance in most catalyst-coated area for $D = 3.0$ cm was around 1.0 mW cm^{-2} (Fig. 3c), which

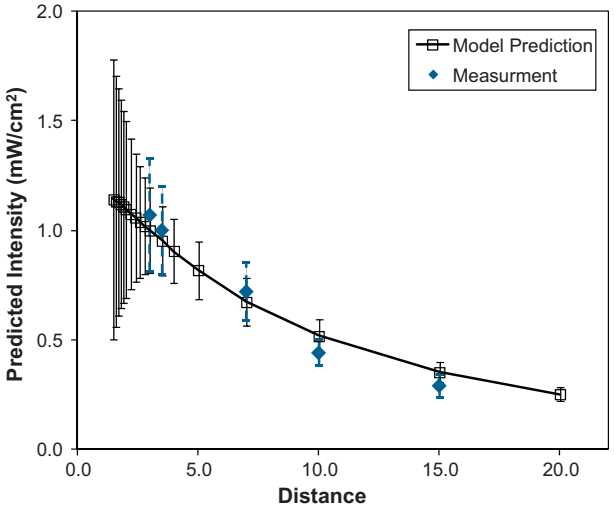

Fig. 4. Model prediction and experimental measurement of the average and standard deviation of the radiation intensity on the surface of the catalyst for different LED positions. The error bars indicate the standard deviations. The predicted averages and standard deviations were calculated from the sufficiently discretized irradiance data generated in the radiation field model. The experimental results were calculated based on at least 20 measurements at randomly-selected different positions on the catalyst surface.

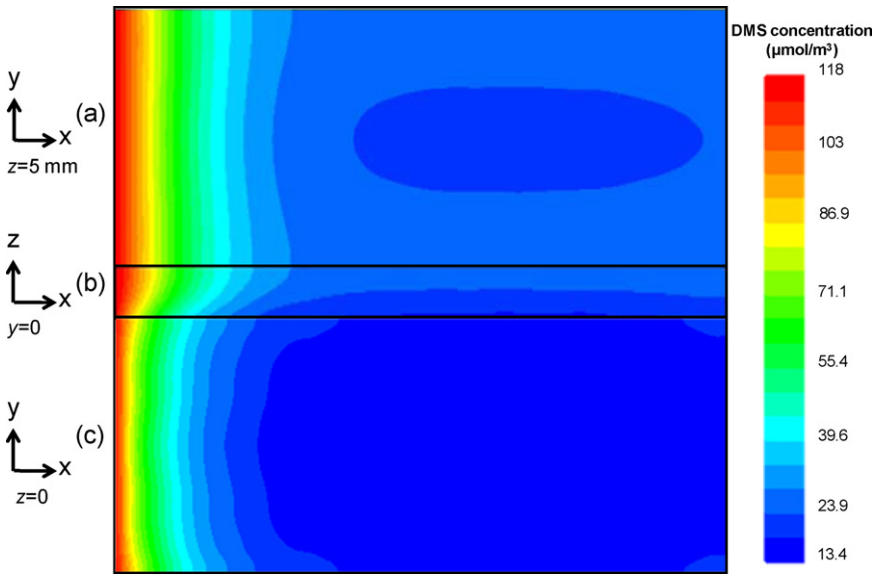

Fig. 5. Contours plot of DMS concentration on the top surface (a), the side surface (b) and the bottom surface of the reactor. The distance between the catalyst thin film and the LED array was 3.0 cm, flow rate = 0.1875 mL/s, inlet DMS concentration = 3.0 ppm.

was the upper bound of the first order regime in the $r \sim I^{\alpha}$ power law relationship.

4.2. Modeling DMS concentration profiles

Fig. 5 shows the steady state concentration profiles of DMS on different surfaces of the reactor predicted by the CFD model for a typical operating condition. The DMS concentration decreased along the axial flow direction due to the decomposition reaction on the catalyst surface (Fig. 5c). The decrease of DMS concentration was more dramatic on the catalyst surface closer to the reactor inlet, because the L–H kinetics was approximately first-order at such low DMS concentrations [34]. Lower DMS concentrations in the center line of the reactor were attributed to the higher radiation intensity in this region (Fig. 5a and c). The DMS concentrations at the side edges of the plate were expected to be lower, since the residence time was longer [7]. However, the concentrations at the side edges were relatively higher, which should be attributed to the lower radiation intensity at the edges (Fig. 3). Fig. 5b shows the vertical and axial DMS concentration profiles on the right side wall of the reactor. The steady-state concentration distribution was developed as a result of advection, diffusion and heterogeneous reaction of DMS in the reactor. The different profiles on the top inner surface and catalyst surface resulted from the difference in the boundary conditions. The vertical gradient at $z = 5$ mm (the inner surface of the quartz cover) was zero because DMS couldn't permeate the upper cover (non-flux boundary condition). Conversely, the positive vertical gradient toward the catalyst film was attributed to the degradation sink of DMS on that surface.

In Fig. 6, DMS removal results predicted at different residence times were compared with the experimental data. As the residence time increased, the conversion increased as expected both in simulation and experimental results. Optimizations of K, k and the form of Eq. (13) could potentially yield better agreement between the model prediction and experimental results, in which the model could be used to (re)evaluate the intrinsic photocatalytic oxidation kinetic parameters. These parameters are more applicable to the design and scale-up of photocatalytic deodorization reactors [7,12].

4.3. Modeling the effect of LED array distance

The selection of LED array configuration and position relative to immobilized catalyst strongly affect the radiation intensity and distribution. Because of the non-linear relationship between radiation intensity and reaction rate, the optimization of LED array design determines the degradation performance and energy efficiency. The optimal radiation power utilization, namely, quantum efficiency, is achieved in the first-order domain [37]. Excessive incident radiation energy will reduce the overall quantum efficiency. For the specific reactor and LED configuration in this study, the challenge is to find an optimal distance between LED array and the catalyst, so that the photon energy can be effectively utilized to achieve optimal DMS removal efficiency. By manipulating the distance parameter, the model simulated the steady state DMS concentration profiles as a function of LED distance (Fig. 7). When the LED array was placed closer to the catalyst plate, the concentration gradients near the discrete strong light spot became more dramatic, where the local reaction rates were relatively higher (Fig. 7b and c). According to

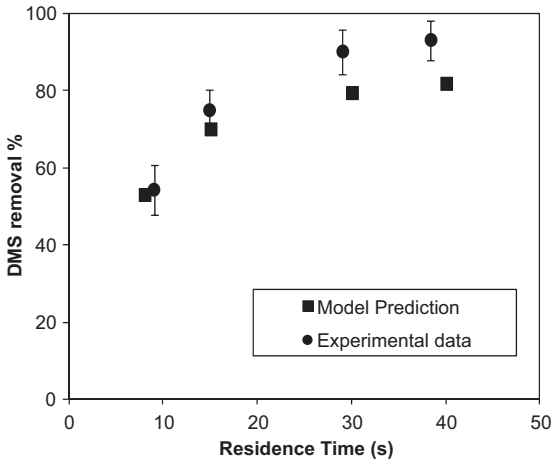

Fig. 6. Comparison of DMS removal efficiency between experimental data and model predictions. The distance between the catalyst thin film and the LED array was 3.0 cm, inlet DMS concentration = 3.0 ppm. The error bars indicates the standard deviations for a minimum replication of three samples.

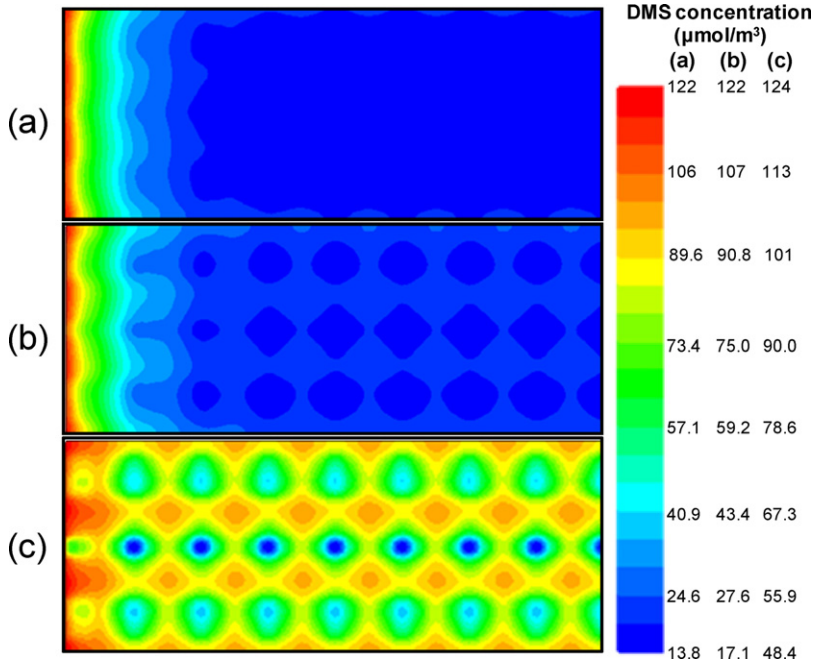

Fig. 7. Contours plot of DMS concentration on the bottom surface ($z = 0$) of the reactor when the LED array was positioned at 1.5 cm (a), 1.0 cm (b) and 0.5 cm (c) above the catalyst plate. Flow rate = 0.1875 mL/s, inlet DMS concentration = 3.0 ppm.

the radiation field model, closer distance resulted in higher heterogeneity of the radiation field. Consequently, the steady state DMS concentration distribution was significantly affected by the radiation field. Interestingly, closer distances (<1.5 cm) yielded lower DMS removal efficiency at the outlet of the reactor, although some local concentrations near the strong light spots were substantially low. It was attributed to the power-law relationship between reaction rate and irradiance defined in this kinetic model. Specifically, the irradiation energy above 1.0 mW cm^{-2} in some areas was not as efficiently utilized for the photocatalytic reaction.

Quantum yield (Φ) is theoretically defined as the number of molecules undergoing an event (conversion of reactants or formation of products) relative to the number of quanta absorbed by the reactant(s) or by the photocatalyst [42]. However, in many practical applications of heterogeneous photocatalysis, the number of absorbed photon is experimentally difficult to measure, due to various optical effects, such as reflection, scattering, and transmission, that may affect the absorption of photons to photocatalyst [43]. In this study, an apparent photonic efficiency (ζ) was defined as the rate of molecules converted (N_r) relative to the total rate of photons incident (N_i) [24,26]. The rate of reaction was calculated based on the mass balance of DMS. Considering the good monochromaticity of the UV-LED, the conversion from photonic energy to the number of photons was estimated based on 365 nm irradiation. Therefore, apparent photonic efficiency is calculated as:

$$\zeta = \frac{N_r\,(mol\ s^{-1})}{N_i\,(einstein\,s^{-1})} = \frac{(C_{in} - C_{out})Q}{\frac{\int\int I_{(x,y)}dxdy}{N_a h\nu}} \quad (14)$$

where C is DMS concentration, Q is volumetric flow rate, ν is the frequency of 365 nm light, N_a and h are Avogadro and Planck constants respectively.

Fig. 8 plots the predicted DMS removal efficiency and apparent photonic efficiency as a function of LED array distance. When the distance was below 1.0 cm, DMS removal efficiency decreased dramatically due to the low photonic efficiency. The poor uniformity of the irradiation distribution leaded to the formation of less reactive regions (the yellow zones in Fig. 7c) on the photocatalyst surface. A distance between 1.5 and 3.0 cm seemed to yield an optimal DMS removal performance, where the radiation field became more uniform and the catalyst surface didn't lose too much total incident photon energy. Further increase of the distance (>3 cm) was predicted to yield a decreased DMS removal efficiency because of stronger dispersion of the radiation field. Anyway, apparent photonic efficiency would keep increasing due to the weaker incident radiation at larger distances. The simulation results demonstrate that the position of the LED light source relative to the catalyst surface is a critical parameter in photocatalytic reactor design.

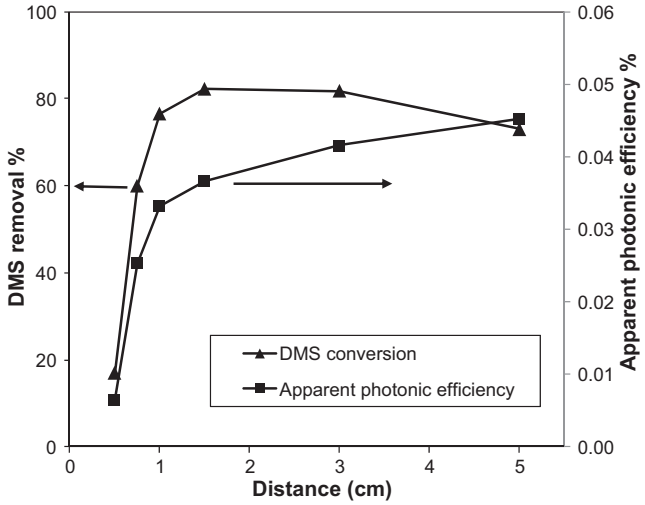

Fig. 8. Model predicted DMS removal efficiency and apparent photonic efficiency as a function of the distance between LED array and catalyst surface. Flow rate = 0.1875 mL/s, inlet DMS concentration = 3.0 ppm.

5. Conclusions

A simple numerical model of a UV-LED based photocatalytic deodorization process in a narrow-slit, plat-plate flow-through

reactor was developed. It combined CFD modeling of the fluid flow in the reactor with radiation field modeling and Langmuir–Hinshelwood reaction kinetics. A non-linear power law relationship between reaction rate and irradiance was adopted in this model. The radiation field model of LED array was able to simulate the irradiation distribution on the catalyst surface as a function of LED configuration and positions. The directivity characteristic of the UV-LED strongly affects the radiation uniformity of the LED array. The CFD model could predict the steady state DMS concentration profile by calculating the advection, diffusion and chemical reaction which is a function of surface DMS concentration and irradiance intensity. The model also showed that the position of LED array relative to the catalyst plate could substantially affect the reactor performance. This study presented a simple example for the modeling of LED array-based photocatalytic process and provided insights to the optimization strategies of LED photocatalytic applications.

Acknowledgments

This work was funded by the Natural Science Foundation of Shanghai (#07ZR14005), the Scientific Research Foundation for the Returned Overseas Chinese Scholars (State Education Ministry), and the Century Star Program of Fudan University. Z.W. received support from Fudan's Undergraduate Research Opportunities Program (FDUROP). The authors thank Prof. Joo-Hwa Tay for his valuable suggestions. The critical comments and suggestions of the anonymous reviewers were very helpful to improve the quality of this manuscript.

References

[1] R. Munoz, R. Lebrero, E. Rodriguez, P.A. Garcia-Encina, A comparative assessment of biofiltration and activated sludge diffusion for odour abatement, J. Hazard. Mater. 190 (2011) 622–630.
[2] J.M. Estrada, N.J.R.B. Kraakman, R. Munoz, R.A. Lebrero, Comparative analysis of odour treatment technologies in wastewater treatment plants, Environ. Sci. Technol. 45 (2010) 1100–1106.
[3] J.H. Mo, Y.P. Zhang, Q.J. Xu, J.J. Lamson, R.Y. Zhao, Photocatalytic purification of volatile organic compounds in indoor air: A literature review, Atmos. Environ. 43 (2009) 2229–2246.
[4] W.K. Jo, S.H. Shin, E.S. Hwang, Removal of dimethyl sulfide utilizing activated carbon fiber-supported photocatalyst in continuous-flow system, J. Hazard. Mater. 191 (2011) 234–239.
[5] M.R. Hoffmann, S.T. Martin, W. Choi, D.W. Bahnemann, Environmental applications of semiconductor photocatalysis, Chem. Rev. 95 (1995) 69–96.
[6] G.B. Raupp, A. Alexiadis, M.M. Hossain, R. Changrani, First-principles modeling, scaling laws and design of structured photocatalytic oxidation reactors for air purification, Catal. Today 69 (2001) 41–49.
[7] I. Salvadó-Estivill, D.M. Hargreaves, G. Li Puma, Evaluation of the intrinsic photocatalytic oxidation kinetics of indoor air pollutants, Environ. Sci. Technol. 41 (2007) 2028–2035.
[8] A.I. Queffeulou, L. Geron, C. Archambeau, H.L. Gall, P.-M. Marquaire, O. Zahraa, Kinetic study of acetaldehyde photocatalytic oxidation with a thin film of TiO_2 coated on stainless steel and CFD modeling approach, Ind. Eng. Chem. Res. 49 (2010) 6890–6897.
[9] F. Taghipour, M. Mohseni, CFD simulation of UV photocatalytic reactors for air treatment, AIChE J. 51 (2005) 3039–3047.
[10] A. Queffeulou, L. Geron, E. Schaer, Prediction of photocatalytic air purifier apparatus performances with a CFD approach using experimentally determined kinetic parameters, Chem. Eng. Sci. 65 (2010) 5067–5074.
[11] F. Taghipour, J.E. Duran, M. Mohseni, Design improvement of immobilized photocatalytic reactors using a CFD-Taguchi combined method, Ind. Eng. Chem. Res. 50 (2011) 824–831.
[12] C. Passalía, O.M. Alfano, R.J. Brandi, A methodology for modeling photocatalytic reactors for indoor pollution control using previously estimated kinetic parameters, J. Hazard. Mater. (2011), doi:10.1016/j.jhazmat.2011.10.007.
[13] S.H. Chong, S.B. Wang, M. Tade, H.M. Ang, V. Pareek, Simulations of photodegradation of toluene and formaldehyde in a monolith reactor using computational fluid dynamics, AIChE J. 57 (2011) 724–734.
[14] C. Passalia, O.M. Alfano, R.J. Brandi, Modeling and experimental verification of a corrugated plate photocatalytic reactor using computational fluid dynamics, Ind. Eng. Chem. Res. 50 (2011) 9077–9086.
[15] J.E. Duran, M. Mohseni, F. Taghipour, Computational fluid dynamics modeling of immobilized photocatalytic reactors for water treatment, AIChE J. 57 (2011) 1860–1872.
[16] I. Salvado-Estivill, A. Brucato, G.L. Puma, Two-dimensional modeling of a flat-plate photocatalytic reactor for oxidation of indoor air pollutants, Ind. Eng. Chem. Res. 46 (2007) 7489–7496.
[17] G.L. Puma, M. Singh, I. Salvado-Estivill, Radiation field optimization in photocatalytic monolith reactors for air treatment, AIChE J. 53 (2007) 678–686.
[18] T.N. Obee, R.T. Brown, TiO_2 Photocatalysis for indoor air applications – effects of humidity and trace contaminant levels on the oxidation rates of formaldehyde toluene, and 1,3-butadiene, Environ. Sci. Technol. 29 (1995) 1223–1231.
[19] H.L. Yu, K.L. Zhang, C. Rossi, Theoretical study on photocatalytic oxidation of VOCs using nano-TiO_2 photocatalyst, J. Photochem. Photobiol. A 188 (2007) 65–73.
[20] S.B. Kim, S.C. Hong, Kinetic study for photocatalytic degradation of volatile organic compounds in air using thin film TiO_2 photocatalyst, Appl. Catal. B 35 (2002) 305–315.
[21] D.H. Chen, X. Ye, K. Li, Oxidation of PCE with a UV LED photocatalytic reactor, Chem. Eng. Technol. 28 (2005) 95–97.
[22] T.S. Natarajan, K. Natarajan, H.C. Bajaj, R.J. Tayade, Energy efficient UV-LED source and TiO_2 nanotube array-based reactor for photocatalytic application, Ind. Eng. Chem. Res. 50 (2011) 7753–7762.
[23] J.-L. Shie, C.-H. Lee, C.-S. Chiou, C.-T. Chang, C.-C. Chang, C.-Y. Chang, Photodegradation kinetics of formaldehyde using light sources of UVA, UVC and UVLED in the presence of composed silver titanium oxide photocatalyst, J. Hazard. Mater. 155 (2008) 164–172.
[24] W.Y. Wang, Y. Ku, Photocatalytic degradation of Reactive Red 22 in aqueous solution by UV-LED radiation, Water Res. 40 (2006) 2249–2258.
[25] J.P. Ghosh, C.H. Langford, G. Achari, Characterization of an LED based photoreactor to degrade 4-chlorophenol in an aqueous medium using coumarin (C-343) sensitized TiO_2, J. Phys. Chem. A 112 (2008) 10310–10314.
[26] H.W. Chen, Y. Ku, A. Irawan, Photodecomposition of o-cresol by UV-LED/TiO_2 process with controlled periodic illumination, Chemosphere 69 (2007) 184–190.
[27] R.J. Tayade, T.S. Natarajan, H.C. Bajaj, Photocatalytic degradation of methylene blue dye using ultraviolet light emitting diodes, Ind. Eng. Chem. Res. 48 (2009) 10262–10267.
[28] M. Izadifard, C.H. Langford, G. Achari, Photocatalytic dechlorination of PCB 138 using leuco-methylene blue and visible light; reaction conditions and mechanisms, J. Hazard. Mater. 181 (2010) 393–398.
[29] S.H. Vilhunen, M.E.T. Sillanpää, Ultraviolet light emitting diodes and hydrogen peroxide in the photodegradation of aqueous phenol, J. Hazard. Mater. 161 (2009) 1530–1534.
[30] Y.L. Kuo, T.L. Su, F.C. Kung, T.J. Wu, A study of parameter setting and characterization of visible-light driven nitrogen-modified commercial TiO_2 photocatalysts, J. Hazard. Mater. 190 (2011) 938–944.
[31] B. Lomans, A. Smolders, L. Intven, A. Pol, H. Op Den Camp, C. Van Der Drift, Formation of dimethyl sulfide and methanethiol in anoxic freshwater sediments, Appl. Environ. Microbiol. 63 (1997) 4741–4747.
[32] I. Devai, R.D. DeLaune, Emission of reduced malodorous sulfur gases from wastewater treatment plants, Water Environ. Res. 71 (1999) 203–208.
[33] K. Demeestere, J. Dewulf, B. De Witte, H. Van Langenhove, Titanium dioxide mediated heterogeneous photocatalytic degradation of gaseous dimethyl sulfide: Parameter study and reaction pathways, Appl. Catal. B 60 (2005) 93–106.
[34] Z. Wang, J. Liu, Y. Dai, W. Dong, S. Zhang, J. Chen, Dimethyl sulfide photocatalytic degradation in a light-emitting-diode continuous reactor: Kinetic and mechanistic study, Ind. Eng. Chem. Res. 50 (2011) 7977–7984.
[35] G. Li Puma, J.N. Khor, A. Brucato, Modeling of an annular photocatalytic reactor for water purification:□ Oxidation of pesticides, Environ. Sci. Technol. 38 (2004) 3737–3745.
[36] W.A. Jacoby, D.M. Blake, R.D. Noble, C.A. Koval, Kinetics of the oxidation of trichloroethylene in air via heterogeneous photocatalysis, J. Catal. 157 (1995) 87–96.
[37] J.M. Herrmann, Heterogeneous photocatalysis: state of the art and present applications, Top. Catal. 34 (2005) 49–65.
[38] V. Puddu, H. Choi, D.D. Dionysiou, G.L. Puma, TiO_2 photocatalyst for indoor air remediation: Influence of crystallinity, crystal phase, and UV radiation intensity on trichloroethylene degradation, Appl. Catal. B 94 (2010) 211–218.
[39] H.L. Yu, K.L. Zhang, C. Rossi, Theoretical study on photocatalytic oxidation of VOCs using nano-TiO_2 photocatalyst, J. Photochem. Photobiol. A 188 (2007) 65–73.
[40] G. Vincent, P.M. Marquaire, O. Zahraa, Abatement of volatile organic compounds using an annular photocatalytic reactor: Study of gaseous acetone, J. Photochem. Photobiol. A 197 (2008) 177–189.
[41] E.N. Fuller, P.D. Schettler, J.C. Giddings, New method for prediction of binary gas-phase diffusion coefficients, Ind. Eng. Chem. 58 (1966) 18–27.
[42] N. Serpone, Relative photonic efficiencies and quantum yields in heterogeneous photocatalysis, J. Photochem. Photobiol. A 104 (1997) 1–12.
[43] R.W. Matthews, S.R. McEvoy, Destruction of phenol in water with sun sand, and photocatalysis, Solar Energy 49 (1992) 507–513.